ELSEVIER

Effect of waveform on the effectiveness of tangential dither forces to cancel friction-induced oscillations

Michael A. Michaux, Aldo A. Ferri*, Kenneth A. Cunefare

School of Mechanical Engineering, The Georgia Institute of Technology, Atlanta, GA 30332-0405, USA

Abstract

High-frequency dither forces are often used to reduce unwanted vibration in frictional systems. This paper examines how the effectiveness of these dither-cancellation techniques is influenced by the nature of periodic signal employed. The paper investigates a single-degree-of-freedom (sdof) system consisting of a mass in frictional contact with a translating belt using two different models of friction. Prior work by the authors focused on sinusoidal dither waveforms. This paper extends this analysis to general, periodic dither forces. Using an averaging technique, the optimal waveforms are determined among periodic signals having either unit-amplitude or unit-rms value. For unit-amplitude dither signals, it is found that square waveforms are able to quench self-excited oscillations with the smallest amplitude of all waveforms of equal strength at every belt speed. Among unit-rms dither waveforms, square waves are best for low belt speeds, but sinusoidal dither is revealed to be best in higher ranges of belt speed. After studying generic waveforms, the results are specialized for three specific examples: sinusoidal, triangular, and square. In particular, the relative performance of the three waveforms is studied using an averaging technique as well as direct time integration.
© 2007 Elsevier Ltd. All rights reserved.

1. Introduction

Recent experimental work at Georgia Tech reported that high-frequency dither forces could suppress squeal in automotive disc brakes [1]. A preliminary analytical and numerical study of this phenomenon treated the brake/caliper system as a mass-on-a-moving-belt problem [2]. The study, which was restricted to sinusoidal dither signals, used numerical integration to simulate the system for a wide range of system and excitation parameters. The simulation results were validated using an analytical averaging technique used recently by Thomsen and co-workers [3–5]. It was found that there was good qualitative agreement between the numerical and analytical results. It was also discovered that, while dither signals can quench friction-induced oscillations, they can also *destabilize* a non-oscillating system if applied incorrectly.

While sinusoidal waveforms are a logical choice for dither signals, numerous alternatives are feasible. Prior research performed using the Georgia Tech brake experiment examined a variety of waveforms (for normal dither). For example, in Ref. [6], dither cancellation was implemented in a "burst mode" in order to reduce the

---

*Corresponding author. Tel.: +1 404 894 7403; fax: +1 404 894 8496.

E-mail address: al.ferri@me.gatech.edu (A.A. Ferri).

power consumption. The burst-waveform was comprised of an "on-segment" followed by an "off-segment." The on segment consisted of a prescribed number of cycles of a particular frequency. The frequency and number of cycles, the relative duration of the on-segment to the off-segment as well as the period of the combined signal, were all varied to determine favorable squeal cancellation. One of the surprising findings of the waveform study was that when the duration of the on-segment was reduced below that of the off-segment, dither was unable to control the brake squeal, regardless of the frequency of the dither on-segment.

Apart from the use of dither in frictional systems, other types of dither waveforms have been studied in reference to a variety of applications. Oldenburger and Nakada [7] compared both triangular and sinusoidal waveforms for stabilization of limit cycles in nonlinear circuits. Their study developed smoothed or "effective characteristics" for the system nonlinearities using the theory of describing functions. Extensions of the describing-function technique may be found in the text by Gelb and Vander Velde [8]. Among the different waveforms considered in Ref. [8] are sine-plus-a-constant, two sines of differing frequency, and random signals. It should be emphasized that, due to the nonlinearities present in the system, the results for a single sinusoid cannot be directly applied to the case of general-periodic or random-input dither. Instead, each waveform must be examined individually to obtain accurate predictions of performance.

In the present paper, the problem of a mass-on-a-moving-belt is further studied. The problem has been used in numerous studies as a simple model of friction-induced vibration in mechanical systems; e.g., Refs. [9–11]. A variety of friction laws have been applied to this problem including Coulomb's law, sticktion (Coulomb's law with differing static and dynamic friction coefficients), and different forms of Stribeck laws. In Ref. [2], two different friction laws were used: one was a cubic-type Stribeck law that had been used by Thomsen [3] and an exponential-based friction law. Since the two laws demonstrated different qualitative behavior when subjected to dither, both laws are considered again in this paper.

The primary purpose of this paper is to examine how the type of dither waveform influences the effectiveness of the dither cancellation technique. The paper first utilizes an analytical technique termed the *method of direct separation of motions* [12], to investigate general, periodic dither waveforms. Through use of the calculus of variations, the analytical results are used to determine optimal waveforms for stabilizing systems with Stribeck and exponentially decreasing friction laws. The generic results are specialized to the case of square and triangular waveforms, for comparison with previously obtained sinusoidal dither results. Emphasis is placed on developing closed-form expressions for effective friction characteristics and for stability predictions. The results of the averaging technique are then validated using numerical integration.

2. Model development

The model used in this paper is very similar to the one used in Ref. [2]; therefore, only a brief description of the model is given here. Fig. 1 shows a spring-mass-damper system resting on a translating surface. The single-degree-of-freedom (sdof) system is subjected to a tangential (i.e., parallel to the sliding surface) dither force denoted as $A_T g(\omega_T t)$, where A_T is the amplitude and g is a zero-mean, periodic waveform. The fundamental frequency of the periodic signal is given by ω_T, which is typically very large compared to the natural frequency and/or the "squeal frequency" of the system. In other words, the dither signal period, $T = 2\pi/\omega_T$, is assumed to be very small in comparison to other relevant time scales. The normal force N and the belt velocity V_0 are assumed to be constant.
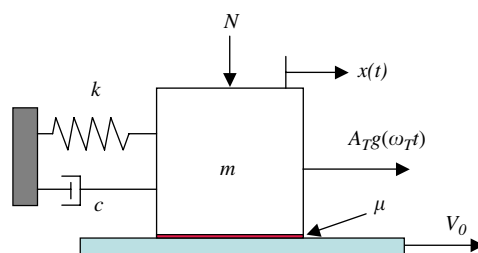

Fig. 1. Sdof model.

The non-dimensional equation of motion of the sdof system is given by

$$\frac{d^2x}{d\tau^2} + 2\zeta\frac{dx}{d\tau} + x = f\left(\frac{dx}{d\tau}\right) + D_T g(R_T\tau), \tag{1}$$

where $\omega_0^2 = k/m$ is the system's natural frequency, $\tau = \omega_0 t$ is non-dimensional time, $\zeta = c/2\omega_0 m$ is the damping ratio, and the tangential dither frequency and amplitude ratios are denoted by $R_T = \omega_T/\omega_0$ and $D_T = A_T/k$, respectively. Note that x and D_T have units of length.

The scaled friction force f is defined as

$$f\left(\frac{dx}{d\tau}\right) = \mu(v_r)F, \tag{2}$$

where $F = N/k$ is a scaled normal force, $v_r = v_0 - dx/d\tau$ is the relative velocity or "slip velocity" of the mass, and v_0 is a scaled belt velocity, $v_0 = V_0/\omega_0$.

2.1. Friction models

2.1.1. Stribeck friction law

The Stribeck friction law [9,10] possesses a low-velocity regime where the friction force magnitude decreases with increasing slip velocity. As the magnitude of the slip velocity increases, the friction function flattens out and then enters a "lubricated regime" where the friction coefficient increases with slip velocity. Although many functional forms have been proposed throughout the literature, the mathematical model used by Thomsen [3–5] is employed here:

$$\mu(v_r) = \begin{cases} \mu_s \operatorname{sign}(v_r) - \frac{3}{2}(\mu_s - \mu_m)\left(\frac{v_r}{v_m} - \frac{1}{3}\left(\frac{v_r}{v_m}\right)^3\right) & \text{for } v_r \neq 0, \\ \tilde{\mu}_s & \text{for } v_r = 0. \end{cases} \tag{3}$$

μ_s can be interpreted as the "static" coefficient of friction, which applies when $v_r = 0$. The parameter μ_m is the minimum coefficient of friction; the slip velocity at which this minimum friction coefficient is attained is denoted v_m. When the interface sticks and $v_r = 0$ for a finite time, the friction force f_s must be determined by equilibrium considerations; this is indicated in Eq. (3) by $\tilde{\mu}_s$, which can be thought of an unknown scaling factor between f_s and the normal load. Note that, unlike many models used in prior frictional studies, the friction coefficient $\mu(v_r)$ can be positive or negative, depending on the instantaneous slip velocity v_r.

2.1.2. Decreasing friction law

While the cubic nature of Eq. (3) lends itself to analytical treatment, the so-called "lubricated regime" of $|v_r| > v_m$ is not appropriate for many frictional systems, including automotive braking systems. Thus, a second friction law is considered in which the friction coefficient smoothly and monotonically decreases with slip velocity:

$$\mu(v_r) = \begin{cases} \left[\mu_m + (\mu_s - \mu_m)\exp\left(-\frac{|v_r|}{v_m}\right)\right]\operatorname{sign}(v_r) & \text{for } v_r \neq 0, \\ \tilde{\mu}_s & \text{for } v_r = 0. \end{cases} \tag{4}$$

The friction coefficient steadily decreases from a static friction coefficient, μ_s, to a value of μ_m, which could be interpreted as the dynamic friction coefficient. In contrast with the Stribeck model (3), the parameter v_m denotes the slip velocity at which $(\mu - \mu_m)$ drops to 36.8% of its initial value $(\mu_s - \mu_m)$. Fig. 2 compares the Stribeck and Decreasing friction models for the case of $\mu_s = 0.4$ and $\mu_m = 0.29$. Note that no effort has been made to match the initial negative slope of the two friction laws. The initial slope of the Stribeck model is $\mu'(0) = -3(\mu_s - \mu_m)/(2v_m)$ while that of the decreasing friction law is $\mu'(0) = -(\mu_s - \mu_m)/v_m$.
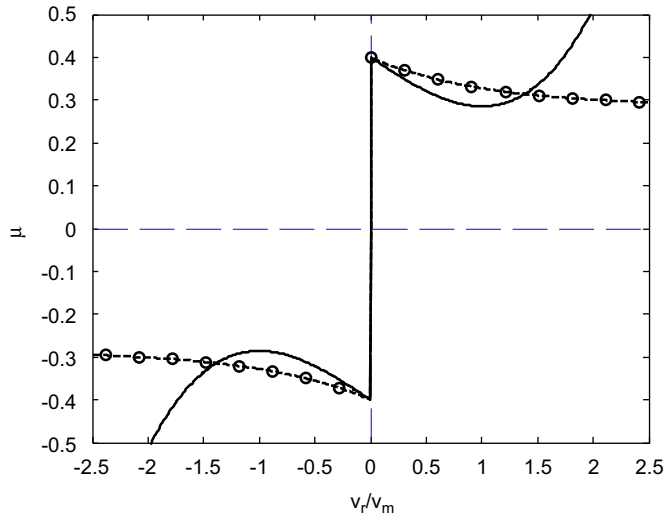
Fig. 2. Comparison of Stribeck and decreasing friction laws; Stribeck ——, Decreasing -○-. Parameters: $\mu_s = 0.4$, $\mu_m = 0.29$.
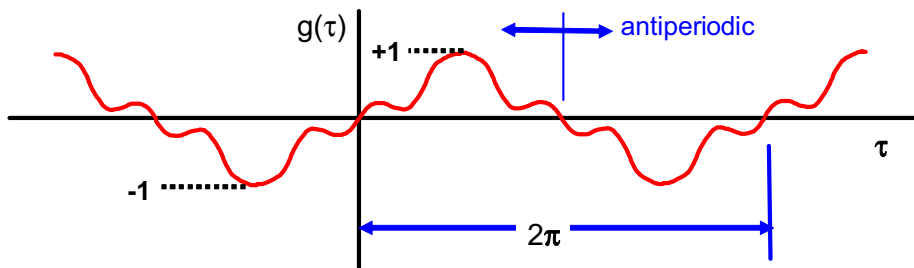

Fig. 3. Possible dither waveform.

2.2. Mathematical form of the dither waveforms

In practice, the form and complexity of a dither waveform are limited only by the fidelity of the power electronics and the dynamics of the force actuator. However, to limit the scope of this study, several assumptions are made regarding the dither signal $g(\tau)$:

1. $g(\tau)$ has zero-mean.
2. $g(\tau)$ is periodic with period 2π.
3. $g(\tau)$ is *antiperiodic* from $[0, \pi]$ versus $[\pi, 2\pi]$; i.e., $g(\tau \pm \pi) = -g(\tau)$.
4. $g(\tau)$ is *odd*; i.e., $g(-\tau) = -g(\tau)$.
5. $g(\tau)$ is strictly greater than zero over $[0, \pi]$ and less than zero over $[\pi, 2\pi]$.

A possible waveform is shown in Fig. 3. Conditions 1–4 imply that $g(\tau)$ can be represented by a Fourier series of the form

$$g(\tau) = \sum_{k=1,3,5,}^{\infty} b_k \sin(k\omega_T \tau). \tag{5}$$

Initially, $g(\tau)$ is assumed to have maximum value 1; later, the case of unit-rms dither signals is also considered. Along with the function itself, the averaging technique requires an integral of the

dither signal:

$$G(\tau) = \int g(\tau)\,\mathrm{d}\tau + C = -\sum_{k=1,3,5,}^{\infty} \frac{b_k}{k\omega_T}\cos(k\omega_T\tau), \tag{6}$$

where the constant of integration C is chosen so that $G(\tau)$ has zero mean.

After deriving the averaged results for the system subject to a generic signal $g(\tau)$ that meets the five assumptions above, the results are specialized to three waveforms: sinusoidal, triangular, and square:

Sinusoidal:

$$g(\tau) = \sin(\tau), \tag{7a}$$

$$G(\tau) = -\cos(\tau). \tag{7b}$$

Triangular:

$$g(\tau) = \begin{cases} \dfrac{2}{\pi}\tau & \text{for } 0 \leqslant \tau \leqslant \dfrac{\pi}{2}, \\[2mm] 2 - \dfrac{2}{\pi}\tau & \text{for } \dfrac{\pi}{2} \leqslant \tau \leqslant \dfrac{3\pi}{2}, \\[2mm] -4 + \dfrac{2}{\pi}\tau & \text{for } \dfrac{3\pi}{2} \leqslant \tau \leqslant 2\pi, \end{cases} \tag{8a}$$

$$G(\tau) = \begin{cases} -\dfrac{\pi}{4} + \dfrac{1}{\pi}\tau^2 & \text{for } 0 \leq \tau \leq \dfrac{\pi}{2}, \\[2mm] \dfrac{\pi}{4} - \dfrac{1}{\pi}(\tau - \pi)^2 & \text{for } \dfrac{\pi}{2} \leq \tau \leq \dfrac{3\pi}{2}, \\[2mm] -\dfrac{\pi}{4} + \dfrac{1}{\pi}(\tau - 2\pi)^2 & \text{for } \dfrac{3\pi}{2} \leq \tau \leq 2\pi. \end{cases} \tag{8b}$$

Square:

$$g(\tau) = \begin{cases} 1 & \text{for } 0 \leqslant \tau \leqslant \pi, \\ -1 & \text{for } \pi < \tau \leqslant 2\pi, \end{cases} \tag{9a}$$

$$G(\tau) = \begin{cases} -\dfrac{\pi}{2} + \tau & \text{for } 0 \leqslant \tau \leqslant \pi, \\[2mm] \dfrac{3\pi}{2} - \tau & \text{for } \pi < \tau \leqslant 2\pi. \end{cases} \tag{9b}$$

3. Analytical treatment using an averaging technique

In this section, the averaging technique used in Refs. [2,3] is generalized to consider a periodic dither signal satisfying assumptions 1–5 above. The solution to Eq. (1) is first decomposed into a fast component, φ, and a slow component, Z:

$$x(\tau) = Z(\tau) + \frac{1}{R_T}\varphi(\tau, R_T\tau). \tag{10}$$

Also, the magnitude of the dither force is assumed to be of the same order as the tangential dither frequency:

$$D_T = \alpha_T R_T \quad \text{with } \alpha_T = O(1), \tag{11}$$

where α_T is termed the strength of the tangential dither signal. Substituting Eq. (10) into Eq. (1), grouping terms, and averaging produces the governing equation for the slow dynamics in terms of the effective friction characteristic, $\bar{\mu}$

$$\ddot{Z} + 2\zeta\dot{Z} + Z + \bar{\mu}(\dot{Z} - v_0)F = 0. \tag{12}$$

Using v_r to denote the slow component of the slip velocity, $\bar{\mu}$ can be expressed as

$$\bar{\mu}(v_r) = \langle \mu(v_r + \alpha_T G(\tau)) \rangle, \tag{13}$$

where $\langle . \rangle$ is the *fast-time-average operator*, which time-averages over one period of the fast excitation, considering the slow time τ to be fixed:

$$\langle f(\tau, R_T \tau) \rangle \equiv \frac{1}{2\pi} \int_0^{2\pi} f(\tau, R_T \tau) \, d(R_T \tau). \tag{14}$$

Eq. (13) applies to any zero-mean dither signal having sufficiently short period and any friction law. In Sections 3.1 and 3.2, the effective friction laws for the two friction models under consideration are worked out in detail. The effective friction laws provide considerable insight into how the discontinuous friction models are smoothed through the effect of high-frequency dither. They can also be used to determine the stability of steady sliding of the sdof system, as shown next.

The equilibrium displacement of the mass in a condition of steady sliding, denoted by $\bar{Z}$, can be obtained by setting $\ddot{Z} = \dot{Z} = 0$ in Eq. (12). This yields

$$\bar{Z} = -\bar{\mu}(-v_0)F. \tag{15}$$

To study the stability of steady sliding, small perturbations about equilibrium are considered, $z(\tau) = Z(\tau) - \bar{Z}$. Inserting $z(\tau)$ into Eq. (12), one obtains

$$\ddot{z} + h(\dot{z}) + z = 0, \tag{16}$$

where the function $h(\dot{z})$ incorporates the effective friction term and the viscous damping term

$$h(\dot{z}) = 2\zeta \dot{z} + F(\bar{\mu}(\dot{z} - v_0) - \bar{\mu}(-v_0)). \tag{17}$$

The system's equivalent linear damping is obtained by taking the first derivative of $h(\dot{z})$. If it is negative, then equilibrium (15) (corresponding to $z = 0$) is unstable, and steady sliding will not be maintained. Ultimately, sustained, limit-cycle oscillations will take place. Thus, the criterion for instability is given by

$$\left. \frac{dh(\dot{z})}{d\dot{z}} \right|_{\dot{z}=0} = 2\zeta + \bar{\mu}'(v_0)F < 0. \tag{18}$$

3.1. Effective friction law for Stribeck friction

The effective friction characteristic for the Stribeck friction law can be obtained by substituting Eq. (3) into Eq. (13):

$$\bar{\mu}(v_r) = \frac{1}{2\pi} \int_0^{2\pi} \left\{ \alpha_0 \, \text{sign}(u) + \alpha_1(v_r + \alpha_T G) + \alpha_3(v_r + \alpha_T G)^3 \right\} d(R_T \tau), \tag{19}$$

where

$$\alpha_0 = \mu_s, \quad \alpha_1 = -\frac{3}{2} \frac{(\mu_s - \mu_m)}{v_m}, \quad \alpha_3 = \frac{1}{2} \frac{(\mu_s - \mu_m)}{v_m^3} \quad \text{and} \quad u = v_r + \alpha_T G.$$

Rearrangement and expansion of Eq. (19) leads to

$$\begin{aligned}
\bar{\mu}(v_r) &= \alpha_0 \langle \text{sign}(u) \rangle + (\alpha_1 \alpha_T + 3\alpha_3 v_r^2 \alpha_T) \langle G \rangle \\
&\quad + \alpha_1 v_r + \alpha_3 v_r^3 + 3\alpha_3 v_r \alpha_T^2 \langle G^2 \rangle + \alpha_3 \alpha_T^3 \langle G^3 \rangle.
\end{aligned} \tag{20}$$

Although not obvious, assumption 3 that the signal $g(\tau)$ be antiperiodic results in the following property:

$$\langle G^n \rangle = 0 \quad \text{for } n = 1, 3, 5, \ldots \,. \tag{21}$$

By Eq. (21), expression (20) simplifies to

$$\bar{\mu}(v_r) = \alpha_0 \langle \text{sign}(u) \rangle + \alpha_3 v_r^3 + (\alpha_1 + 3\alpha_3 \alpha_T^2 \langle G^2 \rangle)v_r. \tag{22}$$
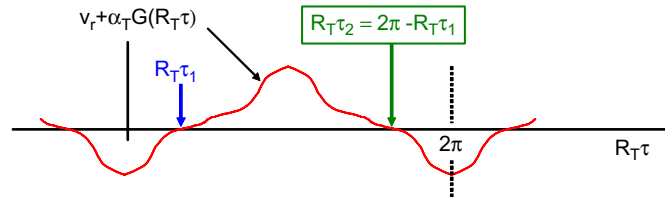
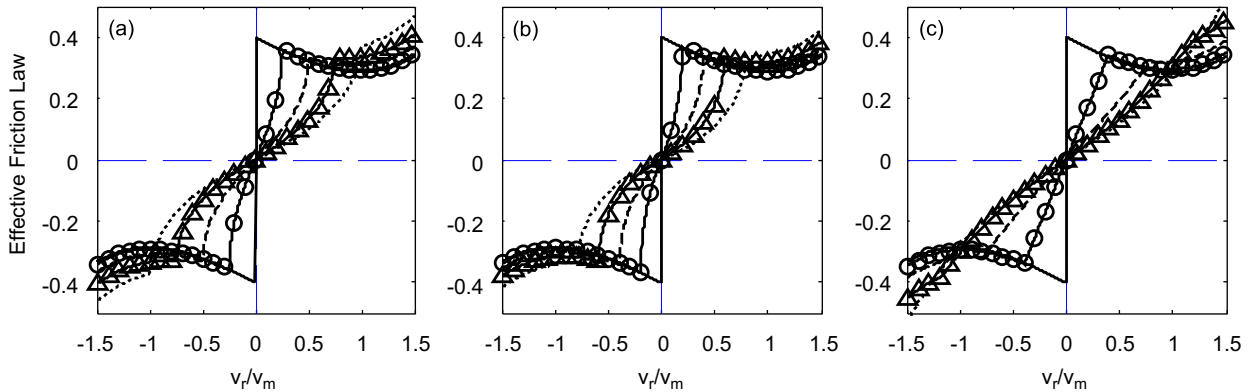Fig. 4. Signum argument for the case $|v_r| \leqslant \alpha_T G_{\max}$.

Fig. 5. Effective Stribeck friction model for three waveforms (a) sinusoidal, (b) triangular, (c) square, for five values of tangential dither strength α_T. Parameters: $\mu_s = 0.4$, $\mu_m = 0.29$. solid line $\alpha_T/v_m = 0$; circles $\alpha_T/v_m = 0.25$; dashed line $\alpha_T/v_m = 0.5$; triangles $\alpha_T/v_m = 0.75$; dotted line $\alpha_T/v_m = 1$.

Note that if $|v_r| > \alpha_T G_{\max}$, where $G_{\max}$ is the maximum value of $G(\tau)$ over $[0, 2\pi]$, then $u = (v_r + \alpha_T G)$ has constant sign for all $R_T \tau$. Conversely, when $|v_r| < \alpha_T G_{\max}$, the sign of u will change over $[0, 2\pi]$ as shown in Fig. 4. Because the signal $g(\tau)$ is assumed to be odd (Assumption 4), $R_T \tau_2 = 2\pi - R_T \tau_1$. Furthermore, because Assumption 5 requires $g(R_T \tau) > 0$ on $[0, \pi]$, $G(R_T \tau)$ is monotonically increasing on $[0, \pi]$ and monotonically decreasing from $[\pi, 2\pi]$; therefore, $R_T \tau_1$ and $R_T \tau_2$ are isolated zero crossings. Thus, it can be shown that the fast-time average of the signum function is given by

$$\langle \text{sign}(v_r + \alpha_T G) \rangle = \begin{cases} 1 - \dfrac{2}{\pi} R_T \tau_1, & |v_r| \leqslant \alpha_T G_{\max}, \\ \text{sign}(v_r), & |v_r| \geqslant \alpha_T G_{\max}. \end{cases} \tag{23}$$

Using Eq. (23), the effective friction characteristic for the Stribeck friction law is given by

$$\bar{\mu}(v_r) = \begin{cases} \alpha_0 \left(1 - \dfrac{2}{\pi} R_T \tau_1 \right) + \alpha_3 v_r^3 + (\alpha_1 + 3\alpha_3 \alpha_T^2 \langle G^2 \rangle) v_r & \text{for } |v_r| \leqslant \alpha_T G_{\max}, \\ \mu(v_r) + 3\alpha_3 \alpha_T^2 \langle G^2 \rangle v_r & \text{for } |v_r| \geqslant \alpha_T G_{\max}. \end{cases} \tag{24}$$

In Appendix A, Eq. (24) is evaluated in closed form for specific cases of sinusoidal, triangular, and square dither waveforms. These effective friction laws are shown in Fig. 5 for five different values of dither strength, assuming that $|g|_{\max} = 1$. Parts (a)–(c) of the figure correspond to the sinusoidal, triangular, and square dither waveforms, respectively. As found previously by Thomsen [3], dither acts to smooth the friction discontinuity in the vicinity of the zero-slip point. As the amplitude of the dither waveform is increased, the discontinuity is smoothed over a wider range of slip velocities. Secondly, it is seen that the slope of effective friction law is dependent both on the amplitude and type of dither waveform. According to condition (18), the degree to which a system is prone to self-excited oscillations is associated with the portions of the curve that have negative slope. It is seen that the effective friction law exhibits a negative slope in the approximate range $\alpha_T G_{\max} < v_r < v_m$. Thus, the higher $G_{\max}$ is, the smaller is the slip-velocity range having negative slope. It is also

seen that, for some level of dither amplitude, the effective friction characteristic is positively sloped over all belt speeds. A comparison of the three plots in Fig. 5 shows that, at each level of dither strength α_T/v_m, the regions of negative slope are greatest for triangular dither, and least for square dither. This observation is further detailed and discussed below.

3.2. Effective friction law for decreasing friction

The effective friction characteristic for the decreasing friction law can be obtained analytically, using Eqs. (4) and (13):

$$\bar{\mu}(v_r) = \frac{1}{2\pi} \int_0^{2\pi} \beta_0 \, \text{sign}(u) + \beta_1 \, \exp\left(-\frac{|u|}{v_m}\right) \text{sign}(u) \, d(R_T \tau), \tag{25}$$

where

$$\beta_0 = \mu_m, \ \beta_1 = \mu_s - \mu_m \quad \text{and} \quad u = v_r + \alpha_T G. \tag{26}$$

Rearrangement of Eq. (25) leads to

$$\bar{\mu}(v_r) = \beta_0 \langle \text{sign}(u) \rangle + \beta_1 \left\langle \exp\left(-\frac{|u|}{v_m}\right) \text{sign}(u) \right\rangle. \tag{27}$$

As before, in an attempt to evaluate Eq. (27) for arbitrary waveforms, two regimes are identified. (For simplicity, it is assumed that the slip velocity is positive; the effective friction law is easily shown to be an odd function of v_r.) For $v_r > \alpha_T G_{\max}$, u has no sign change on $[0, 2\pi]$. In this case, Eq. (27) simplifies to

$$\bar{\mu}(v_r) = \beta_0 + \frac{\beta_1}{\pi} \exp\left(\frac{-v_r}{v_m}\right) \int_0^{\pi} \exp\left(-\frac{\alpha_T G(R_T \tau)}{v_m}\right) d(R_T \tau) \quad \text{for} \quad v_r > \alpha_T G_{\max}. \tag{28}$$

This expression can be evaluated in a closed-form for the specific cases of sinusoidal, square, and triangular waveforms. These expressions may be found in Appendix B. In the regime where $0 < v_r < \alpha_T G_{\max}$, u experiences one sign change on $[0, \pi]$. Using Eq. (23), we can write

$$\bar{\mu}(v_r) = \beta_0 \left(1 - \frac{2}{\pi} R_T \tau_1\right) - \frac{\beta_1}{\pi} \int_0^{R_T \tau_1} \exp\left(\frac{v_r + \alpha_T G(R_T \tau)}{v_m}\right) d(R_T \tau)$$
$$+ \frac{\beta_1}{\pi} \int_{R_T \tau_1}^{\pi} \exp\left(\frac{-v_r - \alpha_T G(R_T \tau)}{v_m}\right) d(R_T \tau). \tag{29}$$

Appendix B gives closed-form expressions from Eq. (29) for the cases of square and triangular waveforms; for the case of sinusoidal waveforms, Eq. (29) requires a numerical evaluation.

Fig. 6 shows a comparison of the effective friction laws for the decreasing friction model for three dither waveforms and for a variety of dither strengths. As in Fig. 5, the dither signals are normalized according to their maximum value, $|g|_{\max} = 1$. There are many similarities between the effective friction law for the decreasing friction model and for the Stribeck model. They all clearly show the mitigating influence of dither for small belt velocities. (Note that the slip velocity is equal to the belt velocity if and when the mass is in a state of steady sliding.) However, in contrast with the curves in Fig. 5, those in Fig. 6 show that the effective friction characteristics never completely lose their regions of negative slope.

4. Stability results

Once the effective friction characteristics have been obtained, the stability can be directly established from Eq. (18), which involves the derivative of $\bar{\mu}(v_r)$. Where closed form expressions exist, the derivative may be calculated analytically (see Appendices A and B); otherwise, the derivative is calculated approximately using finite differences.
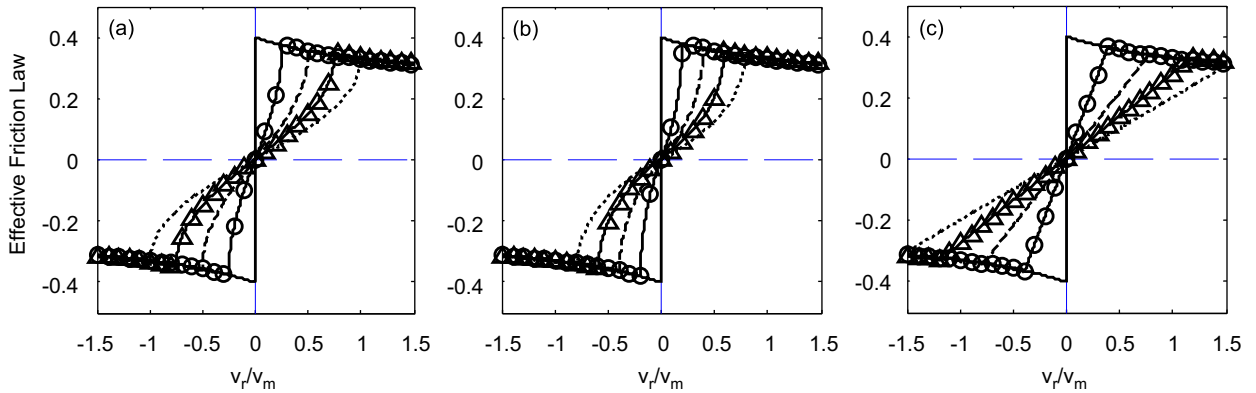
Fig. 6. Effective decreasing friction model for three waveforms (a) sinusoidal, (b) triangular, (c) square, for five values of tangential dither strength α_T. Parameters: $\mu_s = 0.4$, $\mu_m = 0.29$. solid line $\alpha_T/v_m = 0$; circles $\alpha_T/v_m = 0.25$; dashed line $\alpha_T/v_m = 0.5$; triangles $\alpha_T/v_m = 0.75$; dotted line $\alpha_T/v_m = 1$.

4.1. Stability results for Stribeck friction law

For any waveform satisfying Assumptions 1–5, the effective friction characteristic for the Stribeck friction law is given by Eq. (24). Differentiation of Eq. (24) requires knowledge of how changes in v_r affect $R_T \tau_1$:

$$\frac{\mathrm{d}}{\mathrm{d}v_r}(v_r + \alpha_T G(R_T \tau_1)) = 0 \Rightarrow 1 + \alpha_T \frac{\mathrm{d}G}{\mathrm{d}(R_T \tau_1)} \frac{\mathrm{d}(R_T \tau_1)}{\mathrm{d}v_r} = 0. \tag{30}$$

Therefore, since $\mathrm{d}G/\mathrm{d}\tau = g(\tau)$

$$\frac{\mathrm{d}(R_T \tau_1)}{\mathrm{d}v_r} = \frac{-1}{\alpha_T g(R_T \tau_1)}. \tag{31}$$

Using this relation, an expression for the derivative of Eq. (24) can be obtained:
For $|v_r| \leqslant \alpha_T G_{\max}$

$$\bar{\mu}'(v_r) = \frac{2\alpha_0}{\pi \alpha_T g(R_T \tau_1)} + (\alpha_1 + 3\alpha_3 \alpha_T^2 \langle G^2 \rangle) + 3\alpha_3 v_r^2. \tag{32}$$

For $|v_r| > \alpha_T G_{\max}$

$$\bar{\mu}'(v_r) = \mu'(v_r) + 3\alpha_3 \alpha_T^2 \langle G^2 \rangle, \tag{33}$$

where $\mu'(v_r) = 3\alpha_3(v_r^2 - v_m^2)$. Because $\alpha_1 < 0$, it is cumbersome to prove the conditions under which Eq. (32) is positive; by Eq. (18), this is a sufficient condition for stability. For the three waveforms considered in Fig. 5, it may be observed that the slope is positive in the range $|v_r| \leqslant \alpha_T G_{\max}$. More conclusively, Eqs. (32) and (33) show that $\bar{\mu}'(v_r)$ is made *more positive* (or less negative) as $\langle G^2 \rangle$ is increased. In other words, the stability of steady sliding in the system improves as $\langle G^2 \rangle$ increases.

An important observation from Eq. (32) can be made. From Fig. 4, it is first noted that as α_T is increased and approaches $v_r/G_{\max}$, $R_T \tau_1 \to 0$. Since $g(\tau)$ is assumed to be odd, this means that $g(R_T \tau_1) \to 0$, and $\bar{\mu}'(v_r) \to +\infty$. (The possible exception to this occurrence is square waves, for which the value of $g(0)$ is not strictly defined.) This explains why the slope of the effective friction law in Figs. 5(a) and (b) show infinite slope just before v_r exceeds $\alpha_T G_{\max}$. This also suggests a strategy for improving a system's stability of sliding by tailoring the dither signal so that g has a small value at the point where u crosses zero. In other words, the effective friction characteristic can be made to have arbitrarily high, positive slope if $G' = g$ is small at the point where $v_r + \alpha_T G$ crosses zero.

If one assumes that Eq. (32) is positive, then the condition for instability can be obtained by substituting Eq. (33) into Eq. (18) with the slip velocity v_r replaced with the constant belt velocity v_0. For instability in the
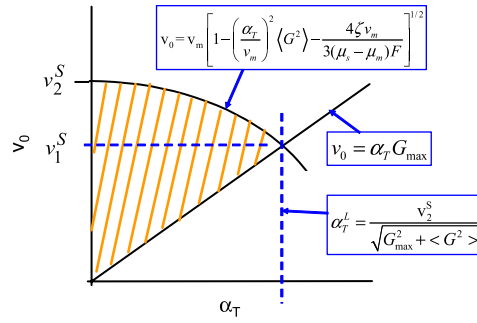
Fig. 7. Stability Bounds and Region.

regime $|v_0| \geqslant \alpha_T G_{\max}$, it is required that

$$2\zeta + F[3\alpha_3(v_0^2 - v_m^2) + 3\alpha_3\alpha_T^2\langle G^2\rangle] < 0. \tag{34}$$

Finally, (34) can be solved for the unstable range of belt velocity:

$$\alpha_T G_{\max} < v_0 < [v_m^2 - \alpha_T^2\langle G^2\rangle - 2\zeta/(3\alpha_3 F)]^{1/2}. \tag{35}$$

Eq. (35) determines the upper and lower bounds of a stability map in the α_T–v_0 plane for the Stribeck friction law. Fig. 7, which shows the general shape and characteristics of the stability region, can be viewed as a generalization of the result for sinusoidal dither first presented by Thomsen in [3]. It is seen that the upper boundary of the unstable region decreases monotonically with α_T. Moreover, the lower bound of the unstable region increases linearly with α_T. This means that, if the undithered system experiences sustained oscillations, there exists a threshold level of dither strength, denoted by α_T^*, that is able to quench the limit-cycle oscillations. Due to the downward sloping upper boundary of the unstable region, one can conclude that it is impossible for a stable system to become destabilized by an increase in the strength of the dither signal. Thus, the stability characteristics for the general dither waveforms considered here are qualitatively the same as those found in [3] for sinusoidal dither in the Stribeck-friction case.

Referring to Fig. 7, it is seen that there is a limiting value of v_0 above which the undithered system ($\alpha_T = 0$) is stable. The limiting value is given by

$$v_2^S = v_m\left[1 - \frac{4\zeta v_m}{3(\mu_s - \mu_m)F}\right]^{1/2} \tag{36}$$

Below v_2^S, we recognize that there are two different ranges of belt speed. For $0 < v_0 < v_1^S$, the dither strength α_T required to stabilize the system increases linearly with v_0; for $v_1^S < v_0 < v_2^S$, the stabilizing dither strength α_T decreases with increasing belt speed. Another feature of the map is a limiting value of α_T beyond which the system is stable for all belt speeds. Denoting this dither amplitude as α_T^L, it can be shown that

$$\alpha_T^L = \frac{v_2^S}{\left[G_{\max}^2 + \langle G^2\rangle\right]^{1/2}}. \tag{37}$$

Finally, as evidenced by (35), the influence of viscous damping is to move the upper bound of the stability region downward, thus reducing the size of the instability region.

Different waveforms can be compared by their influence on the upper and lower bounds of the stability region. The lower bound increases with $G_{\max}$, while the upper bound decreases with $\langle G^2\rangle$. Thus, we seek a waveform that satisfies conditions 1–5, and that simultaneously maximizes $G_{\max}$ and $\langle G^2\rangle$. We distinguish two cases within this optimization problem: unit-amplitude and unit-rms dither waveforms.

Unit Amplitude:

Of all waveforms that satisfy conditions 1–5 above, it is relatively straightforward to determine that the optimal unit-amplitude dither waveform is a square wave. Taking into account the antiperiodicity of $g(\tau)$,

$G_{\max}$ is given by

$$G_{\max} = \frac{1}{2}\int_0^\pi g(\tau)\mathrm{d}\tau = \frac{1}{2}\int_0^\pi G'(\tau)\mathrm{d}\tau, \tag{38}$$

where the factor of $\frac{1}{2}$ originates with the requirement that $G(\tau)$ have a zero-average. If $G_{\max}$ is to be maximized with $|g|_{\max} = 1$, it is clear that $g(\tau)$ should maintain its maximum value over the entire half-period $[0,\pi]$. Thus, the largest possible value for $G_{\max}$ occurs for a unit-amplitude square wave, for which $G_{\max} = \pi/2$.

The general expression for $\langle G^2 \rangle$ is given by

$$\langle G^2 \rangle \equiv \frac{1}{2\pi}\int_0^{2\pi} G^2(R_T\tau)\mathrm{d}(R_T\tau) \tag{39}$$

The requirement that $|g|_{\max} = 1$ places a limit on the *slope* of $G(\tau)$ since $G'(\tau) = g(\tau)$. In order for $G(\tau)$ to have its largest mean-squared value (while maintaining zero mean) $G'(\tau) = +1$ for $0 < \tau < \pi$ and $G'(\tau) = -1$ for $\pi < \tau < 2\pi$. The resulting triangular waveform for $G(\tau)$ yields a mean-squared value of $\langle G^2 \rangle = \pi^2/12$. Thus, we arrive at the conclusion that, of all unit-amplitude dither signals consistent with assumptions 1–5, *the square waveform simultaneously maximizes the lower bound and minimizes the upper bound of the unstable region.*

Unit rms: Another way of normalizing the dither signals is in terms of their rms amplitude. The constraint of unit rms value (or equivalently, unit MS value), can be stated as:

$$MS(g) = \frac{1}{2\pi}\int_0^{2\pi} g^2(\tau)\mathrm{d}\tau = \frac{1}{\pi}\int_0^\pi (G')^2\mathrm{d}\tau = 1. \tag{40}$$

To maximize $G_{\max}$, we must extremize Eq. (38) subject to constraint (40). It may be noted that this is a standard isoperimetric problem in the calculus of variations [13]. The maximizing dither signal $g(t)$ consistent with assumptions 1–5 can be shown to be a unit-amplitude square wave. The maximization of $\langle G^2 \rangle$ is governed by another isoperimetric problem; namely, it is necessary to extremize (39) subject to the isoperimetric constraint (40). The unique result, consistent with assumptions 1-5 is a unit-rms sinewave, $g(\tau) = \sqrt{2}\sin(\tau)$. Therefore, in the case of unit-rms dither signals, the square wave still yields the maximum lower bound of the unstable region. However, *the minimum upper boundary is produced by a unit-rms sinusoidal dither signal.* The results are summarized in Table 1.

The rms-value of a signal is often associated with the signal's "energy." However, it must be noted that the *energy requirement* of the dither cancellation technique depends on the integrated power, defined as the dither force times the absolute velocity of the mass. Comparisons of different dither waveforms in terms of the energy requirement is an interesting, but much more complicated, problem because it depends on the dynamics of the entire system.

To specialize the above discussion to the sinusoidal, triangular, and square waveforms, we need to evaluate $G_{\max}$ and $\langle G^2 \rangle$ for each case. Table 2 summarizes the results. These values can be inserted into Eq. (35) to give specific formulas for each of the three waveforms. Explicit formulas can be found in Appendix A.

Based on the values of $G_{\max}$ for unit-rms waveforms, it is seen that square waves are better than sinusoids and the sinusoids are better than triangular waveforms in raising the lower bound of the unstable region. However, based on the values of $\langle G^2 \rangle$ for unit-rms waveforms, it is seen that sinusoidal dither signals are best. Unit-rms triangular waveforms are nearly as good as sinusoids and unit-rms square waveforms fair worse. The reason is that, of all unit-rms waveforms satisfying assumptions 1–5, the sinusoid focuses all of its energy at a single frequency.

Table 1
$G_{\max}$ and $\langle G^2 \rangle$ dependence on dither waveform

	$G_{\max} = \frac{1}{2}\int_0^\pi g(x)\mathrm{d}x$	$\langle G^2 \rangle \equiv \frac{1}{2\pi}\int_0^{2\pi} G^2(R_T\tau)\mathrm{d}(R_T\tau)$
Unit amplitude dither	Maximized by square wave, $\pi/2$	Maximized by square, $\pi^2/12$
Unit rms dither	Maximized by square wave, $\pi/2$	Maximized by sine wave, 1

Table 2
G_{max} and $\langle G^2 \rangle$ for sinusoidal, square, and triangular waveforms

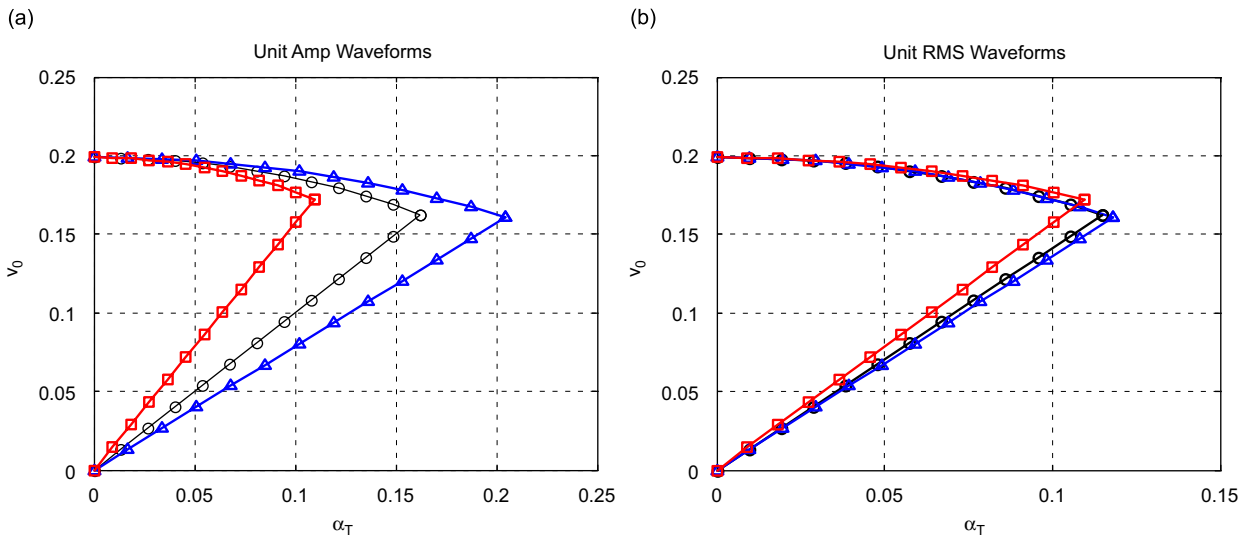| Dither signal	G_{max}	$\langle G^2 \rangle$
Unit amplitude sinewave	1	0.5
Unit amplitude triangular wave	$\pi/4 = 0.7854$	$\pi^2/30 = 0.3290$
Unit amplitude squarewave	$\pi/2 = 1.5708$	$\pi^2/12 = 0.8225$
Unit rms sinewave	$\sqrt{2} = 1.4142$	1
Unit rms triangular wave	$\pi\sqrt{3}/4 = 1.3603$	$\pi^2/10 = 0.9870$
Unit rms squarewave	$\pi/2 = 1.5708$	$\pi^2/12 = 0.8225$

Fig. 8. Stability map for the Stribeck friction model for three waveforms (a) unit amplitude, (b) unit rms; sinusoidal waveform -○-, square waveform -□-, triangular waveform -△-. Parameters: $\zeta = 0.005$, $F = 1$, $v_m = 0.2$, $\mu_s = 0.4$, and $\mu_m = 0.29$.

Fig. 8(a) shows a comparison of the stable region for unit-amplitude sinusoidal, square, and triangular waveforms for the Stribeck friction case. It is seen that there is a significant improvement of sinusoids over triangular waveforms and of square waves over sinusoidal in the unit-amplitude case. In the unit-rms case, shown in Fig. 8(b), it is seen that the relative performance of each waveform shows less variation. That being said, the square waves show best performance for belt speeds lower than v_1^S, and show reasonable performance in the range $v_1^S < v_r < v_2^S$. Assuming that the actuators and power electronics can accommodate square waveforms, they are shown to be a good choice in application to systems exhibiting Stribeck friction characteristics.

4.2. Stability results for decreasing friction law

To determine the stability of the dithered system having a decreasing friction relation, we need the derivative of the effective friction laws shown in Eqs. (28) and (29). For $v_r > \alpha_T G_{max}$, we obtain:

$$\bar{\mu}'(v_r) = \frac{-\beta_1}{v_m \pi} \exp\left(\frac{-v_r}{v_m}\right) \int_0^\pi \exp\left(-\frac{\alpha_T G(R_T\tau)}{v_m}\right) \mathrm{d}(R_T\tau), \tag{41a}$$

$$\bar{\mu}'(v_r) = \frac{-2\beta_1}{v_m \pi} \exp\left(\frac{-v_r}{v_m}\right) \int_0^{\pi/2} \cosh\left(\frac{\alpha_T |G(R_T\tau)|}{v_m}\right) \mathrm{d}(R_T\tau), \tag{41b}$$

where the simplification in Eq. (41b) is made possible by the fact that $G(\pi-\tau) = -G(\tau)$. (For simplicity, v_r is assumed to be positive; the result for $v_r < 0$ is easily obtained by recognizing that the effective friction law is odd.) Inspection of this relation shows that for $v_r > \alpha_T G_{max}$, $\bar{\mu}'(v_r) < 0$ for all waveforms. This may be validated by inspection of Fig. 6, where the slope is noticeably negative when $v_r > \alpha_T G_{max}$. For the limiting value of $v_r = \alpha_T G_{max}$, Eq. (41) takes the form

$$\bar{\mu}'(v_r) = \frac{-\beta_1}{v_m \pi} \exp\left(\frac{-v_r}{v_m}\right) \int_0^\pi \exp\left(-\frac{v_r G(R_T \tau)/G_{max}}{v_m}\right) d(R_T \tau). \tag{42}$$

It is noted that, as v_r increases, $\bar{\mu}'(v_r)$ goes to zero from below, meaning that the sliding state becomes "less prone to instability" as the belt speed is increased. From a practical standpoint, this means that for sufficiently high belt speeds, stable sliding can be assured by very small amounts of viscous damping.

Before one can take the derivative of (29), it must be recalled that τ_1 depends on v_r. Differentiation of the first term in (29) makes use of (31); differentiation of the second term, which involves τ_1 in the integration limits, requires use of Leibnitz's rule. For $0 < v_r < \alpha_T G_{max}$,

$$\bar{\mu}'(v_r) = \frac{2(\beta_0 + \beta_1)}{\pi \alpha_T g(R_T \tau_1)} - \frac{\beta_1}{v_m \pi} \int_0^{R_T \tau_1} \exp\left(\frac{v_r + \alpha_T G(R_T \tau)}{v_m}\right) d(R_T \tau)$$
$$- \frac{\beta_1}{v_m \pi} \int_{R_T \tau_1}^\pi \exp\left(\frac{-v_r - \alpha_T G(R_T \tau)}{v_m}\right) d(R_T \tau). \tag{43}$$

The first term is positive for all dither signals satisfying assumptions 1–5. However, since the integral terms are negative, the derivative $\bar{\mu}'(v_r)$ can be positive or negative in this range of operation.

To assess the stability of the undithered system with a decreasing friction law, we must first set $\alpha_T = 0$ in Eq. (41). This gives

$$\bar{\mu}'(v_r) = \frac{-\beta_1}{v_m} \exp\left(\frac{-v_r}{v_m}\right). \tag{44}$$

Now, using (18), it is found that steady-sliding of the undithered system is unstable for all belt speeds lower than v_2^D given by

$$v_2^D = v_m \ln\left(\frac{F\beta_1}{2\zeta v_m}\right). \tag{45}$$

In [2] is was found that the upper bound of the unstable region is concave up for the decreasing friction law subjected to sinusoidal dither signals. This is confirmed for arbitrary waveforms, if one considers how $\bar{\mu}'(v_r)$ in (41b) changes with α_T. For a given belt speed and dither signal, $\bar{\mu}'(v_r)$ becomes more negative as α_T increases. Therefore if $v_r > v_2^D$, the undithered system will experience steady sliding, but increasing the dither strength runs the risk of making the slope of the effective friction law more negative, thus destabilizing the system. As discussed above, the instability will be avoided if v_r is sufficiently high, and some small amount of viscous damping is present.

The question of "optimal waveforms" follows a similar reasoning to that presented in the context of the Stribeck friction law. The lower bound of the unstable region is given by the line $v_r = \alpha_T G_{max}$; therefore, the optimal waveform is the one that maximizes G_{max}. Whether normalized by unit-rms or unit amplitude, the waveform conforming to assumptions 1–5 that maximizes G_{max} is a square wave.

Because of the concave-up nature of the upper boundary of the unstable region, the question of "optimal" dither waveforms loses its significance. Obviously, for $v_r > v_2^D$, the optimal dither signal to stabilize steady-sliding is zero. However, it is instructive to examine how the dither signal influences the upper boundary of the unstable region. Figs. 9(a) and (b) compare the stable regions for the system with a decreasing friction law for the three different waveforms in the unit-amplitude and unit-rms cases. In the unit-amplitude case, it is seen that the square wave produces the narrowest unstable region of the three waveforms under consideration. It also clearly shows that, for $v_r < v_2^D$, the square waves perform better than the sinusoids, which in turn, outperform the triangular waveforms. However, just as square waves are more efficient at stabilizing steady-sliding, they are also *more efficient at destabilizing steady-sliding* in the decreasing friction case. In the unit-rms
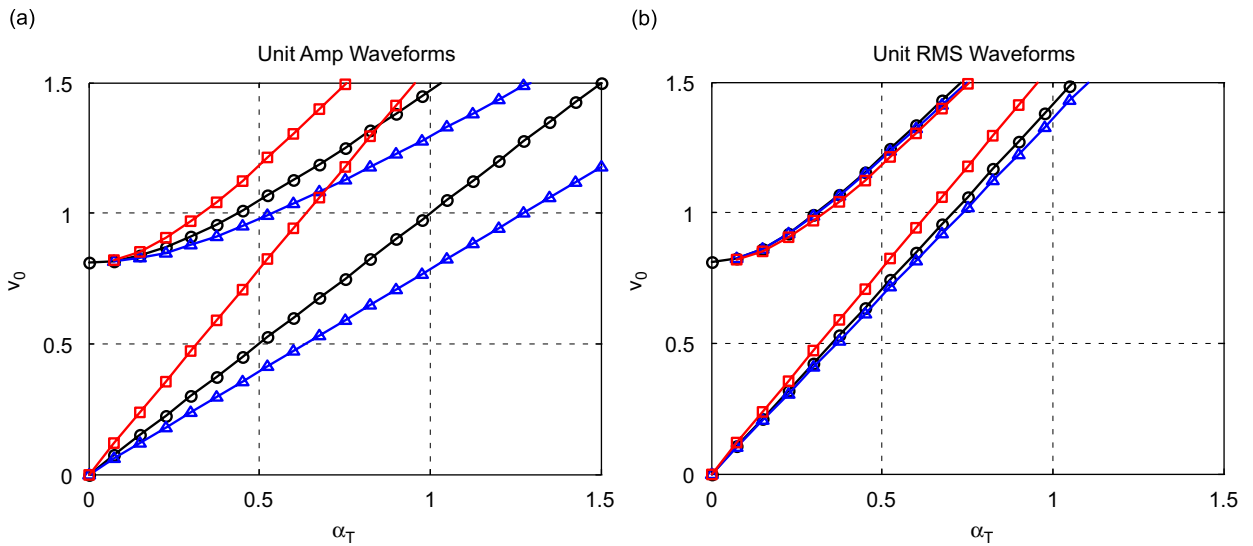
(a)

(b)

Fig. 9. Stability map for the Decreasing friction model for three waveforms (a) unit amplitude (b) unit rms; sinusoidal waveform -○-, square waveform -□-, triangular waveform -△-. Parameters: $\zeta = 0.005$, $F = 1$, $v_m = 0.2$, $\mu_s = 0.4$, and $\mu_m = 0.29$.

case shown in Fig. 9(b), square waves are still clearly better than sinusoidal or triangular waveforms for $v_r < v_2^D$. However, the differences among unit-rms waveforms with respect to the upper boundary of the unstable region are much slighter.

5. Numerical simulation study

The results from the averaging technique can be checked against results obtained from numerical integration. As with all frictional systems, care must be taken in numerical integration routines to deal with numerical stiffness in the vicinity of the discontinuity. In this study, a Runge-Kutta routine is used to directly integrate Eq. (1) during periods of slip. When the slip velocity changes sign and/or becomes sufficiently small, a careful determination of the switching time is determined by backing up and re-integration using smaller time steps. This process is repeated until the switching time converges. Two types of numerical investigations are discussed below. In Section 5.1, simulations are presented that demonstrate the ability of the three types of dither waveforms to eliminate friction-induced oscillations. In Section 5.2, the potential destabilizing influence of dither is demonstrated.

5.1. Cancellation of friction-induced oscillations by dither

Without dither, the sdof system of Fig. 1 is well known to be prone to sustained stick-slip oscillations. For the system and Stribeck friction parameters used in this work, the undithered system settles into a stable limit cycle after a short transient at a fundamental frequency that is close to the natural frequency ($\approx 0.666\omega_0$).

Fig. 10 shows typical numerical simulation results using the Stribeck friction model with $v_0 = 0.05$ and $R_T = 10$. The dashed lines denote the results for the system with no dither and the solid lines show the results for the dithered system with $D_T = 0.4$ ($\alpha_T = 0.04$), and for the three different unit-amplitude waveforms. For triangular dither waveforms, case (a) in Fig. 10, the dithered response shows some amplitude reduction relative to the undithered system. For sinusoidal dither, case (b) in Fig. 10, the response exhibits greater control. The situation depicted in cases (a) and (b) in Fig. 10 is termed "partial control." For square dither waveforms, case (c) in Fig. 10, the system is fully controlled by dither. In other words, the self-excited free-response oscillations are replaced with a forced response at the frequency of the dither input (and its
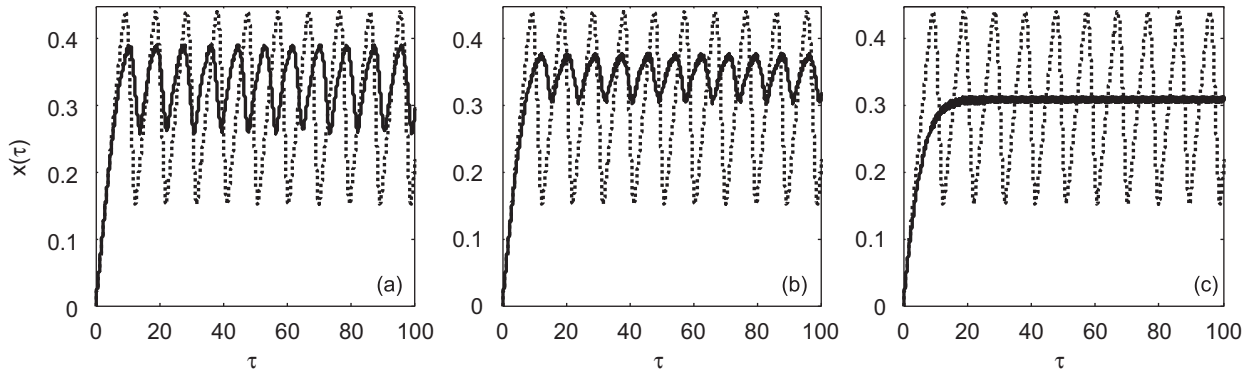
Fig. 10. System displacements $x(\tau)$ with the Stribeck friction model. Reference case without dither excitation ($\cdots$); Dithered system (—). Parameters: $\omega_0 = 1$, $\zeta = 0.005$, $F = 1$, $v_0 = 0.05$, $v_m = 0.2$, $\mu_s = 0.4$, $\mu_m = 0.29$, $R_T = 10$, $D_T = 0.4$, and (a) triangular, (b) sinusoidal, (c) square waveforms.
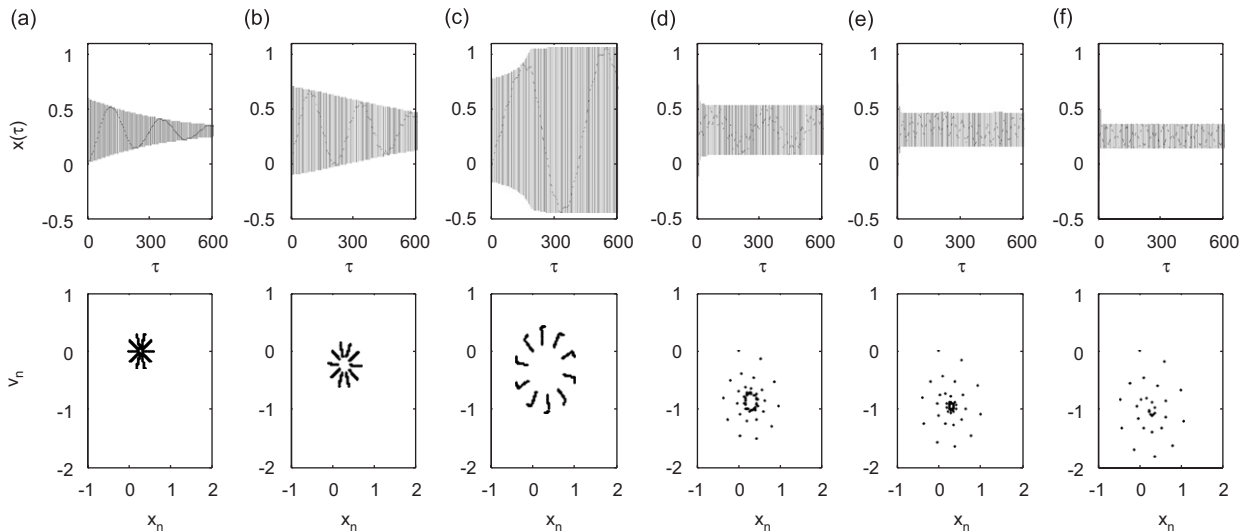

Fig. 11. System responses with the Decreasing friction model, displacements $x(\tau)$ (top row), and Poincaré plots (bottom row) for six values of dither amplitude D_T with triangular waveforms. Parameters: $\omega_0 = 1$, $\zeta = 0.005$, $F = 1$, $v_0 = 1.0$, $v_m = 0.2$, $\mu_s = 0.4$, $\mu_m = 0.29$, $R_T = 10$, and (a) $D_T = 0$, (b) $D_T = 3$, (c) $D_T = 4$, (d) $D_T = 11$, (e) $D_T = 12$, (f) $D_T = 13$.

higher harmonics). Consistent with the results of the averaging method, sinusoidal waveforms achieve a higher level of control than triangular waveforms, but a lower level of control than square waveforms, for a given dither amplitude. The numerical-simulation results of Fig. 10 can be correlated with the stability curves shown in Fig. 8(a). The point $\alpha_T = 0.04$, $v_0 = 0.05$ is well inside the unstable region for the unit-amplitude triangular waveform; it is just inside the unstable region for unit-amplitude sinusoidal waveform. However, for the unit-amplitude square waveform, the point is outside the unstable region.

5.2. Destabilizing effect of dither in the case of the decreasing friction law

As mentioned in Section 4, it is possible to destabilize steady sliding in system with the decreasing friction law by injecting dither into the system. To explore this further, numerical simulations are conducted holding the belt velocity and the dither frequency ratio constant, and observing the response as D_T is increased. For unit-amplitude triangular dither signals, Fig. 11 shows the system response for 6 different values of D_T when the belt velocity is $v_0 = 1$ and $R_T = 10$.

The top row shows the displacement response to zero initial conditions. Note that at $D_T = \alpha_T = 0$, Fig. 9(a) shows that the undithered system is stable. Thus the system should settle into a steady-sliding condition after the transient vibration dies out.

From Fig. 9(a), the averaging method predicts that triangular dither should destabilize steady-sliding for $\alpha_T = 0.54$, i.e. $D_T = \alpha_T R_T = 5.4$. The system should return to a stable state for $\alpha_T > 1.27$, which corresponds to $D_T > 12.7$. Fig. 11 qualitatively validates this behavior. However, steady-sliding becomes unstable at a lower dither amplitude, $D_T \geqslant 4$. Nevertheless, there is agreement with the averaging results for the return to stability prediction, as the system is re-stabilized for dither amplitudes $D_T \geqslant 13$.

The bottom row of plots in Fig. 11 shows the Poincaré plots as D_T changes. The Poincaré section is chosen to coincide with the time instants $R_T \tau_n = 2n\pi$ for $n = 0,1,2,\ldots$. During "stable" response, the Poincaré plot spirals down to a period-1 response. When the dither signal destabilizes the system, the Poincaré plot shows a closed-orbit, closely resembling a period-10 response. It appears that the dither signal is successful in smoothing the nonlinearity, so that the low-frequency response is at or near ω_0, even though the limit-cycle oscillation occurs typically at a lower frequency. In the case of an unstable response, this sustained low-frequency response component is joined to a second component having a period equal to that of the dither signal.

From the numerical simulation shown, and from others generated using other dither waveforms, it is clear that it is possible to destabilize a system through tangential dither, regardless of whether the dither waveform is sinusoidal, triangular, or square. However, it is also seen that, just as unit-amplitude square waveforms are most able to stabilize a self-excited oscillation, they are also most able to destabilize a system in comparison to unit-amplitude triangular and sinusoidal waveforms of the same strength and period.

6. Concluding remarks

Prior work [2] studied the performance of sinusoidal dither waveforms to quench self-excited oscillations in a sdof mass-on-a-moving belt system. The sinusoidal dither study revealed that there were qualitative differences in behavior depending on the friction law. In particular, self-excited oscillations in systems having Stribeck friction (characterized by a high-speed "lubricated regime") are benefited in all cases by tangential dither, as shown originally by Thomsen [3]. However, models incorporating a steadily decreasing friction law were found to be stabilized or destabilized by tangential dither, depending on the belt speed and the dither strength.

This paper extends this result to more-general, periodic dither signals. Two different subclasses are considered: unit-amplitude (i.e., unit peak value) and unit-rms dither signals. The effect of dither waveform on stability is studied using an averaging technique and using direct time-integration. The general results are then specialized to the cases of sinusoidal, triangular, and square dither waveforms.

It is shown that, among all dither signals having the same period and peak-amplitude, square waves have the largest effect on friction-induced oscillations. Furthermore, they produce the smallest region of instability in parameter space. In that sense, they are optimal. This trend was observed for both the Stribeck friction law and the decreasing friction law. Analytical results from an averaging technique show that unit-amplitude sinusoidal waveforms requires a higher dither strength than square waveforms, but a lower strength than triangular waveforms in order to achieve stability of an unstable system, at any belt velocity. This prediction was confirmed using numerical simulations.

The results differed somewhat when the dither signals were normalized by their rms value. In that case, it was found that square waveforms outperform other types of waveforms in some ranges of belt velocity, but sinusoids outperform triangular waveforms, and triangular waveforms outperform square waveforms of equal rms value in other ranges of belt velocity. Overall, it was observed that there was far less variation among the stability regions produced by various unit-rms waveforms than among the stability regions corresponding to various unit-amplitude dither waveforms, regardless of the friction law employed.

Analyses of systems with the decreasing friction law show that it is possible to destabilize steady-sliding through application of general, periodic dither waveforms. This phenomenon, observed previously in the case of sinusoidal dither [2], is not observed in systems using the Stribeck friction model. Both the averaging technique and numerical simulations show that a system that exhibits stable sliding when undithered can be

destabilized by applying dither with triangular and square waveforms of intermediate strength. For a given belt velocity, the range of dither amplitudes that destabilizes the system is broad and within high amplitude levels for the triangular waveforms, and is narrow and within low amplitude levels for the square waveforms. The range of destabilizing dither amplitudes for sinusoidal waveforms lies between that of the triangular and the square waveforms. Also, just as square waves had the best ability to quench self-excited oscillations, they also required the least strength to destabilize steady-sliding among all unit-amplitude waveforms. When normalized by unit-rms value, all three waveforms displayed similar capability to destabilize steady sliding.

Acknowledgments

Appendix A. Effective friction law relations for Stribeck case

This appendix gives a brief development of the effective friction laws and their derivatives for the Stribeck friction case. The reader is referred to [14] for further details. The effective friction characteristic for the Stribeck friction law was given in Eq. (19):

$$\bar{\mu}(v_r) = \frac{1}{2\pi}\int_0^{2\pi}\left\{\alpha_0\mathrm{sign}(u) + \alpha_1(v_r + \alpha_T G) + \alpha_3(v_r + \alpha_T G)^3\right\}\mathrm{d}(R_T\tau), \tag{A.1}$$

where

$$\alpha_0 = \mu_s, \ \alpha_1 = -\frac{3}{2}\frac{(\mu_s - \mu_m)}{v_m}, \ \alpha_3 = \frac{1}{2}\frac{(\mu_s - \mu_m)}{v_m^3}, \quad \text{and} \quad u = v_r + \alpha_T G.$$

As described above, the effective friction characteristic for the Stribeck friction law for any of the three waveforms under consideration is given by

$$\bar{\mu}(v_r) = \begin{cases} \alpha_0\left(1 - \frac{2}{\pi}R_T\tau_1\right) + (\alpha_1 + 3\alpha_3\alpha_T^2\langle G(R_T\tau)^2\rangle)v_r + \alpha_3 v_r^3 & \text{for } |v_r| \leqslant \alpha_T G_{\max} \\ \mu(v_r) + 3\alpha_3\alpha_T^2\langle G(R_T\tau)^2\rangle v_r & \text{for } |v_r| \geqslant \alpha_T G_{\max} \end{cases}. \tag{A.2}$$

The derivative of (A.2) was also derived above for general dither waveforms: For $|v_r| \leqslant \alpha_T G_{\max}$

$$\bar{\mu}'(v_r) = \frac{2\alpha_0}{\pi\alpha_T g(R_T\tau_1)} + (\alpha_1 + 3\alpha_3\alpha_T^2\langle G^2\rangle) + 3\alpha_3 v_r^2 \tag{A.3}$$

For $|v_r| > \alpha_T G_{\max}$

$$\bar{\mu}'(v_r) = \mu'(v_r) + 3\alpha_3\alpha_T^2\langle G^2\rangle, \tag{A.4}$$

where $\mu'(v_r) = 3\alpha_3(v_r^2 - v_m^2)$.

A.1. Sinusoidal dither waveform

In the case of sinusoidal dither, $g(\tau)$ and $G(\tau)$ are given by Eqs. (7a) and (7b), respectively. From these, it can be shown that $G_{\max} = 1$, $R_T\tau_1 = \arccos(v_r/\alpha_T)$, and $\langle G(R_T\tau)^2\rangle = 1/2$. Using these relations, (A.2) reduces to the exact form given by Thomsen [3]:

$$\bar{\mu}(v_r) = \begin{cases} \alpha_0\left(1 - \frac{2}{\pi}\arccos\left(\frac{|v_r|}{\alpha_T}\right)\right)\mathrm{sign}(v_r) + \left(\alpha_1 + \frac{3}{2}\alpha_3\alpha_T^2\right)v_r + \alpha_3 v_r^3 & \text{for } |v_r| \leqslant \alpha_T \\ \mu(v_r) + \frac{3}{2}\alpha_3\alpha_T^2 v_r & \text{for } |v_r| \geqslant \alpha_T \end{cases}. \tag{A.5}$$

A.2. Triangular dither waveform

For the unit-amplitude triangular waveform given in Eqs. (8a) and (8b), it can be shown that $G_{\max} = \pi/4$, $R_T\tau_1 = \sqrt{(\pi^2/4) - (\pi|v_r|/\alpha_T)}$, and $\langle G(R_T\tau)^2\rangle = \pi^2/30$. Using these relations in Eq. (A.2) gives

$$\bar{\mu}(v_r) = \begin{cases} \alpha_0\left(1 - \sqrt{1 - \dfrac{4|v_r|}{\pi\alpha_T}}\right)\mathrm{sign}(v_r) + \left(\alpha_1 + \dfrac{\pi^2}{10}\alpha_3\alpha_T^2\right)v_r + \alpha_3 v_r^3 & \text{for } |v_r| \leqslant \dfrac{\pi}{4}\alpha_T \\[2mm] \mu(v_r) + \dfrac{\pi^2}{10}\alpha_3\alpha_T^2 v_r & \text{for } |v_r| \geqslant \dfrac{\pi}{4}\alpha_T \end{cases}. \tag{A.6}$$

A.3. Square dither waveform

For the unit-amplitude square wave given in Eqs. (9a) and (9b), it can be shown that $G_{\max} = \pi/2$, $R_T\tau_1 = (\pi/2) - (v_r/\alpha_T)$, and $\langle G(R_T\tau)^2\rangle = \pi^2/12$. Using these relations in Eq. (A.2) gives

$$\bar{\mu}(v_r) = \begin{cases} \left(\dfrac{2\alpha_0}{\pi\alpha_T} + \alpha_1 + \dfrac{\pi^2}{4}\alpha_3\alpha_T^2\right)v_r + \alpha_3 v_r^3 & \text{for } |v_r| \leqslant \dfrac{\pi}{2}\alpha_T \\[2mm] \mu(v_r) + \dfrac{\pi^2}{4}\alpha_3\alpha_T^2 v_r & \text{for } |v_r| \geqslant \dfrac{\pi}{2}\alpha_T \end{cases}. \tag{A.7}$$

A.4. Derivatives of the effective friction laws

For the case of $|v_r| > \alpha_T G_{\max}$, Eq. (A.4) shows that the derivative depends only on $\langle G^2\rangle$. These values are listed in Table 2 for unit-amplitude and unit-rms sinusoidal, triangular, and square waveforms. For the case $|v_r| < \alpha_T G_{\max}$, (A.3) can be evaluated in closed-form for each waveform. In addition to $\langle G^2\rangle$, (A.3) also depends on $g(R_T\tau_1)$, which is easily determined in terms of v_r and α_T for each waveform.

Appendix B. Effective friction law relations for decreasing friction case

Equations for the effective friction law, $\bar{\mu}(v_r)$, and for the derivative $\bar{\mu}'(v_r)$ were given above for general dither waveforms conforming to assumptions 1–5. In this appendix, those general equations are specialized for the sinusoidal, square, and triangular waveforms given by Eqs. (7)–(9). (The reader is referred to [14] for further details.) The formulas are specific to the unit-amplitude case, but extensions to the unit-rms case are straightforward. Also, the belt speed is assumed to be positive. The effective friction law for the decreasing friction relation was given in Eq. (27):

$$\bar{\mu}(v_r) = \frac{1}{2\pi}\int_0^{2\pi} \beta_0\mathrm{sign}(u) + \beta_1\exp\left(-\frac{|u|}{v_m}\right)\mathrm{sign}(u)\,\mathrm{d}(R_T\tau), \tag{B.1}$$

where

$$\beta_0 = \mu_m, \quad \beta_1 = \mu_s - \mu_m, \quad \text{and } u = v_r + \alpha_T G. \tag{B.2}$$

For $v_r > \alpha_T G_{\max}$, we obtain

$$\bar{\mu}(v_r) = \beta_0 + \frac{\beta_1}{\pi}\exp\left(\frac{-v_r}{v_m}\right)\int_0^{\pi}\exp\left(-\frac{\alpha_T G(R_T\tau)}{v_m}\right)\mathrm{d}(R_T\tau) \tag{B.3}$$

and

$$\bar{\mu}'(v_r) = -\frac{\beta_1}{\pi v_m}\exp\left(\frac{-v_r}{v_m}\right)\int_0^{\pi}\exp\left(-\frac{\alpha_T G(R_T\tau)}{v_m}\right)\mathrm{d}(R_T\tau). \tag{B.4}$$

For $0 < v_r < \alpha_T G_{\max}$, we obtain

$$\bar{\mu}(v_r) = \beta_0 \left(1 - \frac{2}{\pi} R_T \tau_1\right) - \frac{\beta_1}{\pi} \int_0^{R_T \tau_1} \exp\left(\frac{v_r + \alpha_T G(R_T \tau)}{v_m}\right) \mathrm{d}(R_T \tau)$$
$$+ \frac{\beta_1}{\pi} \int_{R_T \tau_1}^{\pi} \exp\left(\frac{-v_r - \alpha_T G(R_T \tau)}{v_m}\right) \mathrm{d}(R_T \tau), \tag{B.5}$$

and

$$\bar{\mu}'(v_r) = \frac{2(\beta_0 + \beta_1)}{\pi \alpha_T g(R_T \tau_1)} - \frac{\beta_1}{v_m \pi} \int_0^{R_T \tau_1} \exp\left(\frac{v_r + \alpha_T G(R_T \tau)}{v_m}\right) \mathrm{d}(R_T \tau)$$
$$- \frac{\beta_1}{v_m \pi} \int_{R_T \tau_1}^{\pi} \exp\left(\frac{-v_r - \alpha_T G(R_T \tau)}{v_m}\right) \mathrm{d}(R_T \tau), \tag{B.6}$$

B.1. Sinusoidal waveform

For $v_r > \alpha_T G_{\max}$, we obtain

$$\bar{\mu}(v_r) = \beta_0 + \frac{\beta_1}{\pi} \exp\left(\frac{-v_r}{v_m}\right) \int_0^{\pi} \exp\left(\frac{\alpha_T \cos(R_T \tau)}{v_m}\right) \mathrm{d}(R_T \tau). \tag{B.7}$$

A closed-form expression can be obtained for $\bar{\mu}(v_r)$ and $\bar{\mu}'(v_r)$:

$$\bar{\mu}(v_r) = \beta_0 + \beta_1 \exp\left(\frac{-v_r}{v_m}\right) I_o\left(\frac{\alpha_T}{v_m}\right) \tag{B.8}$$

and

$$\bar{\mu}'(v_r) = -\frac{\beta_1}{v_m} \exp\left(\frac{-v_r}{v_m}\right) I_o\left(\frac{\alpha_T}{v_m}\right), \tag{B.9}$$

where I_0 is the modified Bessel function of order zero:

$$I_0(z) = \frac{1}{\pi} \int_0^{\pi} \exp(\pm z \cos(\theta)) \mathrm{d}\theta. \tag{B.10}$$

Eq. (B.9) shows that $\bar{\mu}'(v_r)$ is clearly negative for all belt speeds in the range $v_r > \alpha_T G_{\max}$. For $0 < v_r < \alpha_T G_{\max}$, we obtain

$$\bar{\mu}(v_r) = \beta_0 \left(1 - \frac{2}{\pi} R_T \tau_1\right) - \frac{\beta_1}{\pi} \exp\left(\frac{v_r}{v_m}\right) \int_0^{R_T \tau_1} \exp\left(-\frac{\alpha_T \cos(R_T \tau)}{v_m}\right) \mathrm{d}(R_T \tau)$$
$$+ \frac{\beta_1}{\pi} \exp\left(\frac{-v_r}{v_m}\right) \int_{R_T \tau_1}^{\pi} \exp\left(\frac{\alpha_T \cos(R_T \tau)}{v_m}\right) \mathrm{d}(R_T \tau) \tag{B.11}$$

and

$$\bar{\mu}'(v_r) = \frac{2(\beta_0 + \beta_1)}{\pi \alpha_T g(R_T \tau_1)} - \frac{\beta_1}{v_m \pi} \exp\left(\frac{v_r}{v_m}\right) \int_0^{R_T \tau_1} \exp\left(\frac{-\alpha_T \cos(R_T \tau)}{v_m}\right) \mathrm{d}(R_T \tau)$$
$$- \frac{\beta_1}{v_m \pi} \exp\left(\frac{-v_r}{v_m}\right) \int_{R_T \tau_1}^{\pi} \exp\left(\frac{\alpha_T \cos(R_T \tau)}{v_m}\right) \mathrm{d}(R_T \tau), \tag{B.12}$$

where

$$R_T \tau_1 = \cos^{-1}\left(\frac{v_r}{\alpha_T}\right).$$

Given the form of the integrals, (B.11) and (B.12) are evaluated numerically.

The upper boundary of the unstable region is obtained by substituting Eq. (B.9) into Eq. (18). Steady-sliding is predicted to be unstable in the range

$$G_{\max}\alpha_T < v_r < v_m \ln\left(\frac{F\beta_1 I_0(\alpha_T/v_m)}{2\zeta v_m}\right), \tag{B.13}$$

where $G_{\max} = 1$.

B.2. Square waveform

For $v_r > \alpha_T G_{\max}$, we obtain

$$\bar{\mu}(v_r) = \beta_0 + \frac{\beta_1}{\pi}\exp\left(\frac{-v_r}{v_m}\right)\int_0^\pi \exp\left(-\frac{\alpha_T \pi}{2v_m} + \frac{\alpha_T}{v_m}\tau\right)\mathrm{d}\tau. \tag{B.14}$$

Closed-form expressions can be obtained for $\bar{\mu}(v_r)$ and $\bar{\mu}'(v_r)$:

$$\bar{\mu}(v_r) = \beta_0 + \frac{2\beta_1 v_m}{\pi\alpha_T}\exp\left(\frac{-v_r}{v_m}\right)\sinh\left(\frac{\alpha_T \pi}{2v_m}\right), \tag{B.15}$$

and

$$\bar{\mu}'(v_r) = -\frac{2\beta_1}{\pi\alpha_T}\exp\left(\frac{-v_r}{v_m}\right)\sinh\left(\frac{\alpha_T \pi}{2v_m}\right). \tag{B.16}$$

Eq. (B.16) shows that $\bar{\mu}'(v_r)$ is clearly negative for all belt speeds in the range $v_r > \alpha_T G_{\max}$.

For $0 < v_r < \alpha_T G_{\max}$, $R_T\tau_1 = (\pi/2) - (v_r/\alpha_T)$ and $G(R_T\tau) = -\pi/2 + R_T\tau$ on $[0,\pi]$

$$\bar{\mu}(v_r) = \frac{2\beta_0 v_r}{\pi\alpha_T} - \frac{\beta_1}{\pi}\int_0^{R_T\tau_1}\exp\left(\frac{v_r + \alpha_T(R_T\tau - \pi/2)}{v_m}\right)\mathrm{d}(R_T\tau)$$
$$+ \frac{\beta_1}{\pi}\int_{R_T\tau_1}^\pi \exp\left(\frac{-v_r - \alpha_T(R_T\tau - \pi/2)}{v_m}\right)\mathrm{d}(R_T\tau) \tag{B.17}$$

This is easily evaluated as

$$\bar{\mu}(v_r) = \frac{2\beta_0 v_r}{\pi\,\alpha_T} + \frac{2\beta_1 v_m}{\pi\,\alpha_T}\exp\left(-\frac{\pi\,\alpha_T}{2v_m}\right)\sinh\left(\frac{v_r}{v_m}\right). \tag{B.18}$$

Similarly, evaluation of (B.6) for $\bar{\mu}'(v_r)$ gives

$$\bar{\mu}'(v_r) = \frac{2\beta_0}{\pi\alpha_T} + \frac{2\beta_1}{\pi\alpha_T}\exp\left(-\frac{\pi\alpha_T}{2v_m}\right)\cosh\left(\frac{v_r}{v_m}\right) \tag{B.19}$$

The upper boundary of the unstable region is obtained by substituting Eq. (B.16) into Eq. (18). Steady-sliding is predicted to be unstable in the range

$$G_{\max}\alpha_T < v_r < v_m \ln\left(\frac{F\beta_1}{\pi\zeta\alpha_T}\sinh\left(\frac{\alpha_T \pi}{2v_m}\right)\right), \tag{B.20}$$

where $G_{\max} = \pi/2$.

B.3. Triangular waveform

It is convenient to use the fact that $G(\pi - R_T\tau) = -G(R_T\tau)$ in Eq. (B.3). This gives

$$\bar{\mu}(v_r) = \beta_0 + \frac{\beta_1}{\pi}\exp\left(\frac{-v_r}{v_m}\right)\left\{\int_0^{\pi/2}\exp\left(-\frac{\alpha_T G(R_T\tau)}{v_m}\right)\mathrm{d}(R_T\tau) + \int_0^{\pi/2}\exp\left(+\frac{\alpha_T G(R_T\tau)}{v_m}\right)\mathrm{d}(R_T\tau)\right\}$$

for $v_r > \alpha_T G_{\max}$. From Eq. (8b), $G(R_T\tau) = -(\pi/4) + (\tau^2/\pi)$ on the interval $[0,\pi/2]$. Therefore,

$$\bar{\mu}(v_r) = \beta_0 + \frac{\beta_1}{\pi}\exp\left(\frac{-v_r}{v_m}\right)$$
$$\times \left[\exp\left(\frac{\pi\alpha_T}{4v_m}\right)\int_0^{\pi/2}\exp\left(-\frac{\alpha_T\tau^2}{\pi v_m}\right)\mathrm{d}(R_T\tau) + \exp\left(-\frac{\pi\alpha_T}{4v_m}\right)\int_0^{\pi/2}\exp\left(\frac{\alpha_T\tau^2}{\pi v_m}\right)\mathrm{d}(R_T\tau)\right],$$

or

$$\bar{\mu}(v_r) = \beta_0 + \frac{\beta_1}{2}\sqrt{\frac{v_m}{\alpha_T}}\exp\left(\frac{-v_r}{v_m}\right)\left[\exp(\gamma)\mathrm{erf}(\sqrt{\gamma}) + \exp(-\gamma)\mathrm{erfi}(\sqrt{\gamma})\right], \tag{B.21}$$

where $\gamma = \pi v_m/4\alpha_T$ and

$$erf(z) = \frac{2}{\sqrt{\pi}}\int_0^z\exp(-z^2)\mathrm{d}z \ \text{ and } \ \mathrm{erfi}(z) = \frac{2}{\sqrt{\pi}}\int_0^z\exp(+z^2)\mathrm{d}z.$$

Differentiation of (B.19) with respect to v_r yields

$$\bar{\mu}'(v_r) = -\frac{\beta_1}{2\sqrt{\alpha_T v_m}}\exp\left(\frac{-v_r}{v_m}\right)\left[\exp(\gamma)\mathrm{erf}(\sqrt{\gamma}) + \exp(-\gamma)\mathrm{erfi}(\sqrt{\gamma})\right]. \tag{B.22}$$

Eq. (B.22) shows that $\bar{\mu}'(v_r)$ is clearly negative for all belt speeds in the range $v_r > \alpha_T G_{\max}$.

For $0 < v_r < \alpha_T G_{\max}$, we start again with (B.5):

$$\bar{\mu}(v_r) = \beta_0\left(1 - \frac{2}{\pi}R_T\tau_1\right) - \frac{\beta_1}{\pi}\int_0^{R_T\tau_1}\exp\left(\frac{v_r + \alpha_T G(R_T\tau)}{v_m}\right)\mathrm{d}(R_T\tau)$$
$$+ \frac{\beta_1}{\pi}\int_{R_T\tau_1}^{\pi/2}\exp\left(\frac{-v_r - \alpha_T G(R_T\tau)}{v_m}\right)\mathrm{d}(R_T\tau)$$
$$+ \frac{\beta_1}{\pi}\int_{\pi/2}^{\pi}\exp\left(\frac{-v_r - \alpha_T G(R_T\tau)}{v_m}\right)\mathrm{d}(R_T\tau), \tag{B.23}$$

where $R_T\tau_1 = (\pi/2)\sqrt{1 - (4v_r/\pi\alpha_T)}$. The limits of the third integral can be modified using the fact that $G(\pi - R_T\tau) = -G(R_T\tau)$:

$$\bar{\mu}(v_r) = \beta_0\left(1 - \frac{2}{\pi}R_T\tau_1\right) - \frac{\beta_1}{\pi}\int_0^{R_T\tau_1}\exp\left(\frac{v_r + \alpha_T G(R_T\tau)}{v_m}\right)\mathrm{d}(R_T\tau)$$
$$+ \frac{\beta_1}{\pi}\int_{R_T\tau_1}^{\pi/2}\exp\left(\frac{-v_r - \alpha_T G(R_T\tau)}{v_m}\right)\mathrm{d}(R_T\tau) + \frac{\beta_1}{\pi}\int_0^{\pi/2}\exp\left(\frac{-v_r + \alpha_T G(R_T\tau)}{v_m}\right)\mathrm{d}(R_T\tau).$$

Substituting that $G(R_T\tau) = -(\pi/4) + (\tau^2/\pi)$ on the interval $[0, \pi/2]$, we get

$$\bar{\mu}(v_r) = \beta_0(1 - 2R_T\tau_1/\pi) + \frac{\beta_1}{2}\sqrt{\frac{v_m}{\alpha_T}}\exp\left(-\frac{v_r}{v_m}\right)\exp(\gamma)\left\{\mathrm{erf}(\sqrt{\gamma}) - \mathrm{erf}(\delta)\right\}$$
$$- \frac{\beta_1}{2}\sqrt{\frac{v_m}{\alpha_T}}\exp\left(\frac{v_r}{v_m}\right)\exp(-\gamma)\mathrm{erfi}(\delta) + \frac{\beta_1}{2}\sqrt{\frac{v_m}{\alpha_T}}\exp\left(-\frac{v_r}{v_m}\right)\exp(-\gamma)\mathrm{erfi}(\sqrt{\gamma}), \tag{B.24}$$

where $\delta = (2R_T\tau_1/\pi)\sqrt{\gamma}$. A similar procedure to evaluate (B.6) yields

$$\bar{\mu}'(v_r) = \frac{2(\beta_0 + \beta_1)}{\pi\alpha_T g(R_T\tau_1)} - \frac{\beta_1}{2\sqrt{\alpha_T v_m}}\exp\left(-\frac{v_r}{v_m}\right)\exp(\gamma)\left\{\mathrm{erf}(\sqrt{\gamma}) - \mathrm{erf}(\delta)\right\}$$
$$- \frac{\beta_1}{2\sqrt{\alpha_T v_m}}\exp\left(\frac{v_r}{v_m}\right)\exp(-\gamma)\mathrm{erfi}(\delta) - \frac{\beta_1}{2\sqrt{\alpha_T v_m}}\exp\left(-\frac{v_r}{v_m}\right)\exp(-\gamma)\mathrm{erfi}(\sqrt{\gamma}). \tag{B.25}$$

The upper boundary of the unstable region is obtained by substituting Eq. (B.22) into Eq. (18). Steady-sliding is predicted to be unstable in the range

$$G_{\max}\alpha_T < v_r < v_m \ln\left(\frac{F\beta_1}{4\zeta\sqrt{\alpha_T v_m}}\left[\exp(\gamma)\mathrm{erf}(\sqrt{\gamma}) + \exp(-\gamma)\mathrm{erfi}(\sqrt{\gamma})\right]\right), \tag{B.26}$$

where $G_{\max} = \pi/4$.

References

[1] K.A. Cunefare, A.J. Graf, Experimental active control of automotive disc brake rotor squeal using dither, *Journal of Sound and Vibration* 250 (4) (2002) 579–590.

[2] M.A. Michaux, A.A. Ferri, K.A. Cunefare, Effect of tangential dither signal on friction induced oscillations in an sdof model, *ASME Journal of Computational and Nonlinear Dynamics* 2 (3) (2007) 201–210.

[3] J.J. Thomsen, Using fast vibrations to quench friction-induced oscillations, *Journal of Sound and Vibration* 228 (5) (1999) 1079–1102.

[4] J.J. Thomsen, A. Fidlin, Analytical approximations for stick-slip vibration amplitude, *International Journal of Non-Linear Mechanics* 38 (2003) 389–403.

[5] J.J. Thomsen, Some general effects of strong high-frequency excitation: stiffening, biasing and smoothening, *Journal of Sound and Vibration* 253 (4) (2002) 807–831.

[6] M. Dzirasa, Experimental investigation of dither control for the suppression of automotive brake squeal, MS Thesis, G.W. Woodruff School of Mechanical Engineering, Georgia Institute of Technology, Atlanta, GA, 30332-0405, 2002.

[7] R. Oldenburger, T. Nakada, Signal stabilization of self-oscillating systems, *IRE Transactions on Automatic Control, AC* 6 (3) (1961) 319–325.

[8] A. Gelb, A.W. Vander Velde, *Multiple-input describing functions and non-linear system design*, McGraw-Hill, New York, 1968.

[9] R.A. Ibrahim, Friction-induced vibration, chatter, squeal, and chaos—part I: mechanics of contact and friction; —part II: dynamics and modeling, *Applied Mechanics Reviews* 47 (7) (1994) 209–253.

[10] B.P. Armstrong-Hélouvry, P. Dupont, C. Canudas De Wit, A survey of models, analysis tools and compensation methods for the control of machines with friction, *Automatica* 30 (7) (1994) 1083–1138.

[11] U. Andreaus, P. Casini, Dynamics of friction oscillators excited by a moving base and/or driving force, *Journal of Sound and Vibration* 245 (4) (2001) 685–699.

[12] I.I. Blekhman, *Vibrational mechanics: nonlinear dynamic effects, general approach, applications*, World Scientific Press, Singapore, 2000.

[13] R. Weinstock, *Calculus of variations with applications to physics and engineering*, Dover Publications, New York, 1974.

[14] M.A. Michaux, Suppression of friction-induced oscillations through use of high-frequency dither signals, PhD Thesis, G.W. Woodruff School of Mechanical Engineering, Georgia Institute of Technology, Atlanta, GA, 2005.